RESEARCH ARTICLE
PLANETARY SCIENCES

Earth and Planetary Physics
7: 1–15, 2023
doi: 10.26464/epp2023036

Constraints on water activity at the Zhurong landing site in Utopia Planitia, Mars

ChengZheng Yong[1,2], ZiYao Fang[1,2*], CongCong Zhang[1,2,3], JunFeng Zhen[1,2,3], and LiPing Qin[1,2]

[1]Deep Space Exploration Laboratory/Chinese Academy of Sciences Key Laboratory of Crust-Mantle Materials and Environments, University of Science and Technology of China, Hefei 230026, China;

[2]Chinese Academy of Sciences Center for Excellence in Comparative Planetology, Hefei 230026, China;

[3]Chinese Academy of Sciences Key Laboratory for Research in Galaxies and Cosmology, Department of Astronomy, University of Science and Technology of China, Hefei 230026, China

Key Points:

- Hydrated minerals have been identified at the Zhurong landing site.
- Groundwater may have resulted in the formation of hydrated minerals.
- Active aqueous activities occurred during the Amazonian era on Mars.

Citation: Yong, C. Z., Fang, Z. Y., Zhang, C. C., Zhen, J. F., and Qin, L. P. (2023). Constraints on water activity at the Zhurong landing site in Utopia Planitia, Mars. *Earth Planet. Phys.*, *7*(3), 1–15. http://doi.org/10.26464/epp2023036

Abstract: Mineralogical evidence of water–rock interactions is a strong indicator of the presence of liquid water on ancient Mars. Previous observations have found widely distributed hydrated minerals in the southern highlands, whereas such discoveries have been rare in the younger northern lowlands. China's first Mars exploration mission successfully landed a rover (Zhurong) in southern Utopia Planitia, providing an opportunity to analyze the exposed rocks in the northern lowlands. Using data from the short-wave infrared (SWIR) spectrometer and the laser-induced breakdown spectrometer (LIBS) onboard the Zhurong rover, we found evidence for the widespread presence of hydrated minerals (probably sulfates or silica) around the landing site. The basaltic-like elemental compositions of the targeted samples further indicated that hydrated minerals are likely minor components. The results from Zhurong suggest that active aqueous activities occurred during the overall cold and dry Amazonian era on Mars. However, further evaluations are needed on the duration and scale of these activities.

Keywords: Zhurong rover; hydrated mineral; water activity; Amazonian

1. Introduction

Water is a prerequisite for the emergence of life. Although modern Mars is hyperarid and has little evidence of the presence of liquid water, it is widely thought that the surface environment of early Mars was mild and might have been rich in liquid water (Fassett and Head, 2011). Evidence for aqueous environments on early Mars includes fluvial valley networks, ancient water-related sedimentary landforms, and mineralogical fingerprints of interaction with water (Ehlmann and Edwards, 2014; McLennan et al., 2019; Dickson et al., 2021).

Several kinds of minerals provide strong evidence for the presence of water on Mars. Phyllosilicates, such as smectite and kaolinite, are products of the aqueous alteration of igneous silicate minerals. The widespread phyllosilicates in the southern highlands present evidence for early aqueous weathering and hydrothermal and diagenetic environments during the Noachian (Ehlmann and Edwards, 2014). Phyllosilicates are relatively scarce in the Hesperian and Amazonian. A global change may have occurred at the Noachian–Hesperian boundary, leading to more arid environments, which made sulfates the dominant alteration products during the Hesperian (Head et al., 2002; Bibring et al., 2006; Johnson et al., 2008). Several explanations have been proposed for the formation mechanisms of sulfates on Mars: progressive evaporation of brines (Clark and Van Hart, 1981; Bridges and Grady, 2000), acidic groundwater circulation (Burns and Fisher, 1990; Gendrin et al., 2005), hydrothermal activity (Newsom et al., 1999; Bishop et al., 2005), impact-generated weathering (Knauth and Burt, 2004; Cloutis et al., 2006), the interaction of volcanic aerosols with surface minerals (Settle, 1979; Cloutis et al., 2006), and the alteration of mafic minerals from rain, frost, or both through volcanic outgassing (Bullock et al., 2004; Gendrin et al., 2005). In most scenarios, water is required for the formation of sulfates. Therefore, the detection and identification of sulfates can provide a perspective on water activity as well as the paleoclimate on Mars. Hydrated silica is another possible indicator of aqueous activity. It has been found in some young deposits in late Hesperian or even Amazonian strata (Milliken et al., 2008; Lee et al., 2015). Hydrated

First author: C. Z. Yong, yongchengzheng@mail.ustc.edu.cn
Correspondence to: Z. Y. Fang, fzy@ustc.edu.cn
Received 03 NOV 2022; Accepted 08 MAR 2023.
Accepted article online 31 MAR 2023.

silica minerals have been proposed as the product of several processes, including sedimentary deposition, altered ash deposition (Milliken et al., 2008), acidic leaching (Bishop et al., 2008), thin coatings from volcanic exhalation (Minitti et al., 2007), and precipitation from Si-rich water (Skok et al., 2010; Ruff et al., 2011; Bandfield et al., 2013). In some cases, hydrated silica is found to be accompanied by sulfates and clay minerals (Bishop et al., 2008; Milliken et al., 2008; Ruff et al., 2011), indicating complex formation conditions. Moreover, opal-A, the amorphous phase with the least aqueous alteration among opal types, should convert completely to quartz within ~400 Ma when exposed to aqueous environments (Tosca and Knoll, 2009). Therefore, it can be used as an indicator of the duration of water activity.

The orbital observations and several Mars landing missions over the past two decades have revealed a wide distribution of water-related minerals, including phyllosilicates, sulfates, chlorides, and silica, in the southern highlands at low and middle latitudes (Ehlmann and Edwards, 2014), whereas these minerals are rare and mainly confined to large craters in the northern lowlands, showing the excavated strata 1–2 km beneath surface materials (Pan L et al., 2017; Pan L and Ehlmann, 2018). Because the northern lowlands are mainly covered by Martian dust, the exposure of potential indigenous water-related minerals may be restricted, which can obscure their identification from orbital observations. Therefore, *in situ* geochemical and mineralogical investigation on the surface of the northern lowlands is important to fill in the blank in orbital observations. In 1976, the X-ray fluorescence spectrometer onboard both the Viking 1 and 2 landers, which landed at Chryse Planitia and Utopia Planitia, respectively, detected moderate S concentrations in four samples of Martian fines, and model results showed possible ~10% sulfates in the samples (Baird et al., 1976). The gas chromatograph–mass spectrometer onboard the Viking 1 lander demonstrated the presence of H_2O in two surface samples collected from the Chryse Planitia region of Mars by heating the samples to 500 °C (Biemann et al., 1976).

As part of the Tianwen-1 mission, the Zhurong rover successfully landed in southern Utopia Planitia at 25.066°N, 109.925°E at an elevation of –4,099.4 m on May 15, 2021 (Liu J et al., 2022). The rover has six scientific payloads. Here, we used data from the Mars Surface Composition Detector (MarSCoDe) on board the Zhurong rover to study the compositions of surface materials around the landing site. The MarSCoDe consists of a laser-induced breakdown spectrometer (LIBS) and a short-wave infrared (SWIR) spectrometer (Xu WM et al., 2021), designed to detect elemental emission lines and obtain reflectance spectra, respectively. The LIBS is capable of detecting most major elements (e.g., Si, Al, Ca, Fe, Mg, Na, K) and possibly some minor elements (Zou YL et al., 2021). The SWIR spectrometer is sensitive to the diagnostic absorption peaks of various minerals, including the absorption peaks of hydrated minerals at 1.4, 1.9, and ~2.2 μm. With the two techniques combined, the MarSCoDe is capable of identifying the types and compositions of surface materials, especially those related to water activity, to gain a more comprehensive understanding of the geologic history of Utopia Planitia.

2. Geologic Background of Utopia Planitia

Utopia Planitia is the largest recognized impact basin in the northern lowlands of Mars (McGill, 1989). This terrain is overlain by the Late Hesperian-aged Vastitas Borealis Formation (VBF) materials and was resurfaced by the Amazonian-aged deposits associated with Elysium (Head et al., 2002; Tanaka et al., 2014). The absolute model age of the landing site is 757 ± 66 Ma, as estimated by crater counting, indicating a Middle Amazonian age of the uppermost layer (Zhao JN et al., 2021). The Zhurong rover is now heading to the highland–lowland boundary, in the vicinity of suspected ancient shorelines (Liu JJ et al., 2022).

Utopia Planitia contains many geologic features, including craters, pitted cones, mesas, ridges, troughs, fractures, and transverse aeolian ridges (Mills et al., 2021; Wu X et al., 2021; Ye BL et al., 2021; Liu JJ et al., 2022; Huang H et al., 2023), showing abundant geologic events and erosion in the history. The concentric grabens, also known as ghost craters, are proposed to be the result of volcanic deposits or wet sediment filling in ancient impact craters (Buczkowski and Cooke, 2004). Along with layered ejecta craters, they might indicate that subsurface volatiles could have existed (Wu X et al., 2021). Abundant pitted cones have been found around the landing area, possibly formed by mud volcanoes (Ivanov et al., 2014; Ye BL et al., 2021). Other formation mechanisms are possible, such as cinder cones (Lanz et al., 2010) and pingos (de Pablo and Komatsu, 2009). These pitted cones in Utopia Planitia lack flow-like features at their flanks, compared with the pitted cones in Acidalia Planitia interpreted as mud volcanoes (Wu X et al., 2021). Further *in situ* analysis by the rover may give additional information about the origin. A ground-penetrating radar survey of the subsurface structure in the landing area found no liquid water within the detection depth, but the radar suggests a multi-layered structure below the regolith, which may have been formed by episodic hydraulic flooding sedimentation during the Late Hesperian to Amazonian (Li C et al., 2022).

3. Methods

3.1 SWIR Spectroscopy

The SWIR spectrometer onboard the Zhurong rover has a spectral range of 850–2,400 nm with 321 bands (311 bands in practice) and uses an acousto-optic tunable filter (AOTF) crystal as the dispersive component. The spectral resolution varies from 3 to 12 nm, and the field of view is 36.5 mrad (Xu WM et al., 2021). The passive mode of the MarSCoDe instrument collects the radiance reflected from targets in units of watts per square meter per steradian per spectral band. To obtain the reflectance of each target, it also needs to collect the radiance from two calibration panels with 99% and 40% of reflectivity.

The offset for the wavelength shift caused by the AOTF temperature was described in Wu B et al. (2022) as follows:

$$Y_{1,400} = 0.0861T - 7.9742, \quad (1)$$

$$Y_{2,000} = 0.1141T - 6.8022, \quad (2)$$

where $Y_{1,400}$ and $Y_{2,000}$ are offsets (nm) at two characteristic atmosphere absorption centers, calculated from the difference between the modeled CO_2 absorption center and that of science data, and T is the AOTF temperature. By using the two anchors, the offsets at all wavelengths can be fitted linearly as follows:

$$\text{Offset}_i = \text{Gain} \times X_i + \text{Bias}, \quad (3)$$

where Offset_i is the correction value at wavelength X_i, and Gain and Bias are the slope and intercept of the fitted linear equation, which are

$$\text{Gain} = (Y_{1,400} - Y_{2,000})/(X_{1,400} - X_{2,000}), \quad (4)$$

$$\text{Bias} = (Y_{1,400}X_{2,000} - Y_{2,000}X_{1,400})/(X_{2,000} - X_{1,400}), \quad (5)$$

where $X_{1,400}$ and $X_{2,000}$ are center wavelengths of the corresponding absorption features.

The reflectance of each target is derived by applying the following equation (Hu XY et al., 2019):

$$\text{REFF}_{\text{sample}} = I_{\text{sample}}/I_{\text{plaque}} \times \text{REFF}_{\text{plaque}}. \quad (6)$$

In this equation, $\text{REFF}_{\text{sample}}$ is the reflectance of the target, $\text{REFF}_{\text{plaque}}$ is the laboratory-measured reflectance value of the calibration panel, and I_{sample} and I_{plaque} are the radiance of the target and the calibration panel, respectively, after the aforementioned correction. Only the white panel (99% reflectivity) was used in this work. We then applied the Savitzky–Golay algorithm (Savitzky and Golay, 1964) with 19 points and a fifth polynomial order to denoise the spectra. This algorithm is based on fitting successive subsets of adjacent data points with polynomials. The unsmoothed spectra are shown in Figure S1.

3.2 LIBS

The LIBS onboard the Zhurong rover was used to detect the elemental compositions of surface materials with a stand-off distance of 1.6–7 m (Xu WM et al., 2021). The central wavelength of the output laser is 1,064 nm. The spectral range of the LIBS detector is 240–850 nm. It consists of three channels (240–340 nm, 340–540 nm, and 540–850 nm), with spectral resolutions of 0.067, 0.133, and 0.2 nm, respectively. The spectral range can cover most of the emission lines of elements of interest. The laser spot at a distance of 5 m is approximately 0.18 mm. An assembly of 12 standard samples is installed on the orientation antenna mast of the rover for the calibration of LIBS spectra.

The acquired LIBS spectra were first calibrated for wavelength through the emission lines of the Ti alloy standard material from the calibration assembly. Every spectrum was then normalized by integrating the entire emission spectrum. Elements were identified by their diagnostic emission lines in the spectra. For semiquantitative estimation of the element ratios, the background of a certain emission line was subtracted by fitting the lowest signals on either side of the peak. The area of the emission line was then integrated with approximately the range of the width at half maximum. As regards the emission line for Al at ~396.15 nm, the peak overlapped the peak for Ca at ~396.85 nm; thus, a multi-Gaussian fitting method was used to separate the two peaks before integrating the peak area.

4. Results

4.1 Observation of Geologic Features

The route traveled by the Zhurong rover is generally flat, with several crescent-shaped transverse aeolian ridges (Figures 1 and 2; Lu Y et al., 2022). Images from the Navigation and Terrain Camera (NaTeCam) showed that different kinds of rocks are distributed along the traverse (Figure 2). Some rocks are angular and dark toned, and these are likely basaltic rocks excavated by impacts (Figure 2a; Liu Y et al., 2022). Other rocks are light toned, with a color similar to the soils in the area. These rocks are mostly covered by dust and have various shapes and textures. Some of them are rock pieces on the ground with peeling or pitted surfaces (Figures 2b, 2c), indicating possible physical erosion by wind or other surface alteration processes. Layered structures can also be observed on some of these light-toned rocks (Figure 2b). A type of platy rock is widely distributed along the traverse of the rover (Figure 2d, 2e). These rocks are much larger than the rock pieces and have slab structures with no clear angle. They are mostly buried in the soil and dispersed slightly over the ground. Fractures can be seen on most of these rocks. The color of these platy rocks is almost indistinguishable from that of the soils, suggesting that the local soils may have been derived from these rocks. All these kinds of rocks were continuously observed by the rover. Different kinds of rocks, as well as aeolian ridges and soils, were analyzed by the MarSCoDe along the traverse of the rover.

4.2 SWIR Characterization of Minerals

Several absorption bands in the SWIR spectra can be used to identify hydrated minerals. The absorption band at 1.40–1.48 μm is caused by the overtone of OH stretching, and the absorption feature near 1.94 μm is due to the combination of the H–O–H bending and the OH stretching (Clark, 1999). Other characteristics can also specifically distinguish certain hydrated minerals, such as 1.85 μm for OH combinations in jarosite, 2.1 μm for H_2O stretching plus H_2O rotating in monohydrated sulfates, 2.2 μm for the combination of OH stretching and SiOH or SiOSi bending in opals, and 2.265 μm for combinational OH stretching and Fe–OH bending in jarosite (Cloutis et al., 2006; Liu Y et al., 2018). The precise position of a band may vary depending on the cation type and mineral structure, which is a subtle feature that can be used to distinguish different types of hydrated minerals (Liu Y et al., 2018).

The processed SWIR spectra from the Zhurong rover and the laboratory-measured references are shown in Figure 3. The slopes, shapes, and absorption features are quite similar among most of these *in situ* spectra. They show considerable drops at 1.94 μm and subtle features at 0.94 and 2.22–2.23 μm. Some spectra show very subtle absorptions at 1.75 μm. The obvious absorption feature at 1.94 μm suggests the presence of hydrated minerals. However, the specific types of minerals remain an open question because of the low signal-to-noise ratio (40–55 decibels before correction and calibration; Xu WM et al., 2021). The absorption features at ~1.94 and ~2.23 μm may be related to those in opaline silica and sulfate minerals (specifically opal-A and Ca- and Mg-sulfates; Figure 3). Opal-A has a distinctive ~1.9–1.91 μm absorption peak as well as a double peak at 2.21 and 2.26 μm, although it is hard to distinguish the double peak in the Zhurong data because of relatively low signal-to-noise ratios. Compared with opaline silica, the 1.94 μm band positions seem to be more consistent with Ca-sulfates (anhydrite, gypsum, or bassanite). However, in spectra of Sol 43, Sol 47, and Sol 58, the ~1.94 μm absorption centers are at a shorter wavelength, closer to that of opaline silica. It is difficult to attribute the 2.23 μm feature to opaline silica or Ca-

sulfates, and it is difficult to find minerals corresponding to the 2.3 μm feature. If the spectra collected by Zhurong unexpectedly shifted to a longer wavelength, the 2.3 μm absorption might be attributed to Ca-sulfates. Furthermore, it is difficult to distinguish polyhydrated Mg-sulfates (epsomite, starkeyite) from Ca-sulfates. Therefore, the SWIR spectra can best be explained by opaline silica or sulfates, but we are unable to identify the specific minerals.

4.3 LIBS Detection of Elements

The LIBS spectra from the Zhurong rover are essentially similar until sol 110. Two typical LIBS spectra are shown in Figure 4. A few peaks for major elements are marked (Figure 4). The ultraviolet range is rich in emission lines. Those around 240 and 260 nm are predominantly from Fe, and the peaks around 252 nm overlap the emission lines from Fe and Si. Several lines from Mg around 280 nm and a Si line at 288.16 nm are also prominent in this range. The violet range is characterized by two Ca lines at 393.37 and 396.85 nm, which are the most prominent peaks in the entire spectra. Between these two peaks are two relatively weak peaks for Al at 394.40 and 396.15 nm. The relative intensities of peaks in the visible and near-infrared range are weaker than those from the performance testing in the simulated Martian environment before launch (Xu WM et al., 2021), but emission lines for Na (~589 nm), K (766.49 and 769.90 nm), O (~777 and ~845 nm), and Ca (854.21 and 866.21 nm) are clear in this range.

All the spectra with sufficient signal-to-noise ratios have an obvious emission line from H at ~656.5 nm (Figure 5). This peak overlaps that of the C line at ~658 nm. We found no evidence of the presence of carbonates in the studied area, and this C line exists in almost every Martian LIBS spectrum with a sufficient signal-to-noise ratio from Zhurong, as well as in published data from the Curiosity rover in the Gale crater (Meslin et al., 2013; Nachon et al., 2014; Schröder et al., 2015; Rapin et al., 2016). Thus, the C line is most likely from the breakdown of CO_2 in the atmosphere (Rapin et al., 2016). Quantitative analysis of H is difficult because of the presence

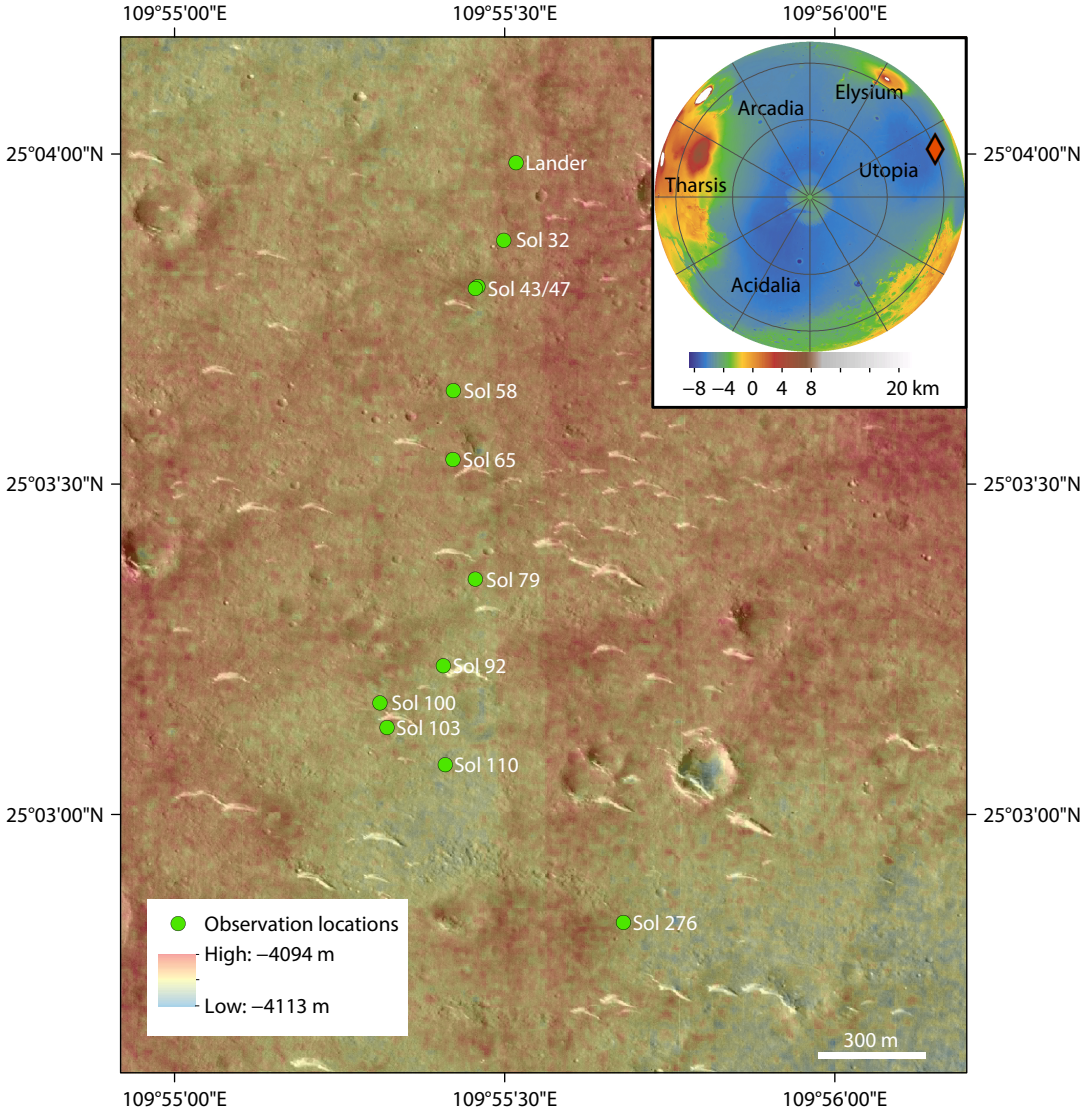

Figure 1. Geologic map of the traverse of the Zhurong rover. The base map is a High-Resolution Imaging Camera (HiRIC) image (~0.7 m per pixel) overlain by a HiRIC digital terrain model (~3.5 m per pixel) (Table S1). The green dots are observation locations of the Zhurong rover. The red diamond shows the landing site.

of matrix effects, a dark spectrum, and the stark effect, among others (see Schröder et al., 2015, for details). In this study, we discuss the presence of H in the targets qualitatively only. Because the H peak exists in every spectrum, including those from the reference samples (Figure 5), it does not necessarily indicate that all the targeted samples contain hydrated minerals. Rapin et al. (2016) suggested that normalization of the H peak to the O peak or C peaks could be used to estimate the water content in samples. For convenience of comparison, we used the relative intensity of the H peak to the C peak at ~658 nm as an indicator. A notably higher peak for H at ~656.5 nm than the C peak at ~658 nm was defined as "strong evidence for the presence of H" in this study. In this view, 6 out of 25 spectra with accepted signal-to-noise ratios had obvious signals from H (Figure 5), suggesting the presence of hydrated minerals.

The relative intensities of emission lines can be used for semi-quantitative estimation of the relative abundances of elements. From the analysis of SWIR spectra, sulfates and opaline silica are the most likely hydrated minerals in the targets. On Mars, Ca and Mg are common cations in sulfates, and Si is the major element in opaline silica. Additionally, Ca and Mg are mobile elements during water-induced weathering (Nesbitt and Wilson, 1992). Thus, we use Ca, Mg, and Si to trace the addition of sulfate evaporites and silica, or the loss of elements during weathering. Aluminum is a relatively immobile element and can be used to estimate the detrital contributions. Therefore, normalization to Al can be used to suggest the depletion or enrichment of Ca, Mg, and Si relative to the pristine igneous rocks. The ratios of the integrated areas of emission lines from Ca, Mg, Si, and Al are shown in Figure 6. The Ca/Al and Si/Al ratios of most samples show only small variations, whereas the Mg/Al ratios show relatively larger variations, which may suggest that Mg sulfates are the main hydrated minerals in the samples. However, we found no systematic difference between those with obvious H emission lines and others. Additionally, the targets that were interpreted to be basaltic rocks (Sol 45-1 and Sol 50-1; Liu Y et al., 2022) had elemental ratios similar to those of other samples (Figure 6). The elemental ratios of all samples also did not deviate significantly from those of the basalt reference. All these results suggest that the depletion or addition of Ca, Mg, and Si is likely not significant in the targets. Therefore, the elemental compositions of the targets may be similar to those of basaltic materials, and the hydrated minerals may be only minor components in the samples.

5. Discussion

5.1 Evidence for Water Activity at Utopia Planitia

The absorption bands of H_2O and OH from the SWIR spectra clearly suggest the presence of hydrated minerals in the targets, probably sulfates or opaline silica. The detection of H in LIBS spectra further supports this interpretation. Even though hydrated minerals are present, it is important to assess whether they are indeed indigenous or from hydrated components in the Martian dust (Hamilton et al., 2005; Yen et al., 2005). A ubiquitous H emission line was identified in the LIBS spectra of the fine-grained soil in the Gale crater analyzed by the Curiosity rover, corresponding to hydrated phases (Meslin et al., 2013). This fine-grained soil was thought to represent the globally dispersed Martian dust (Meslin

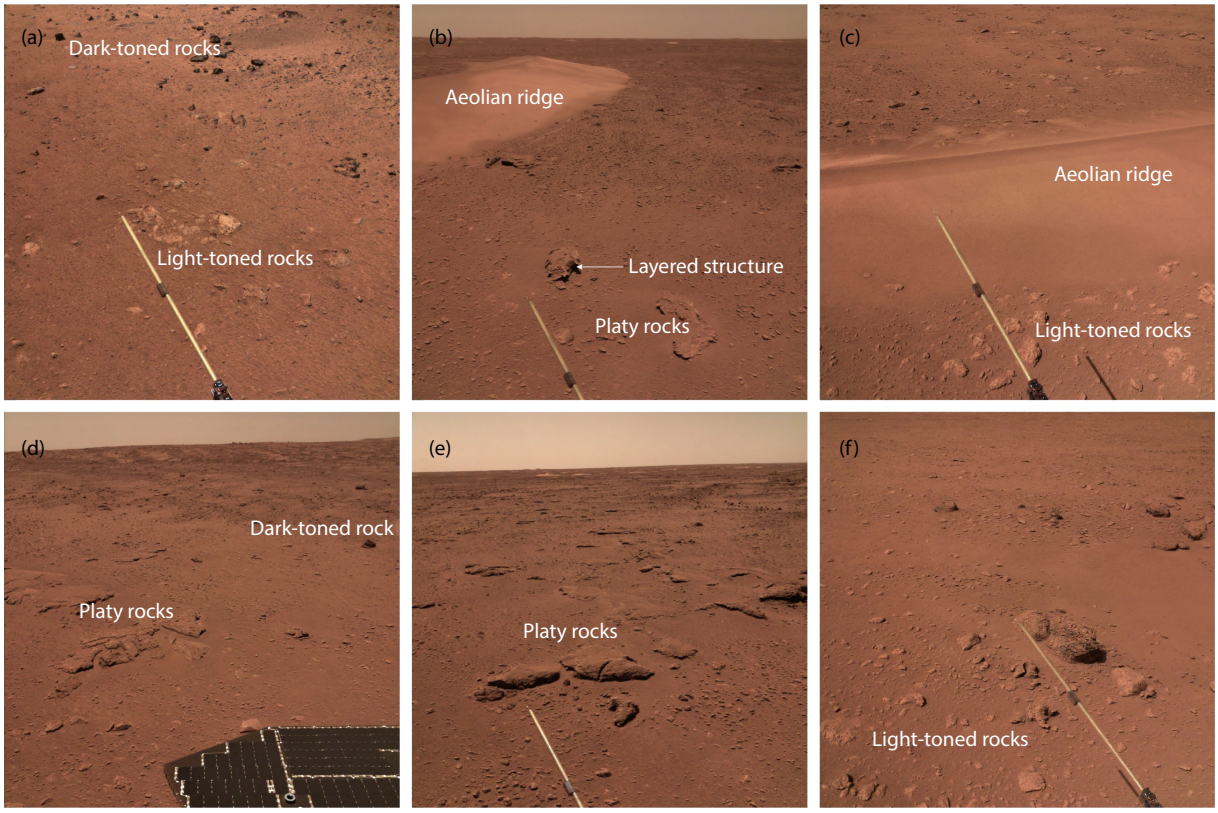

Figure 2. Different geologic features along the traverse of the rover shown by images from the Navigation and Terrain Camera (NaTeCam) (Table S2).

et al., 2013). Thus, data from the MarSCoDe may be affected by the signal from the Martian dust. However, it is unlikely that Martian dust could account for all the identified features of hydrated minerals. Because the laser pulses during LIBS analyses could remove dust and expose the surface of the rocks within the initial several shots, further shots would reveal the elemental compositions under the surface (up to 400 μm for the LIBS onboard the Curiosity rover; Maurice et al., 2016). Therefore, for the rock targets, the dust would have a limited influence on the detection of elements, and the hydrated features (such as the high H peak in the spectrum of Sol 32-2; Figure 5) are likely from the rocks, indicative of indigenous origin.

Sulfates and opaline silica have been found at many locations on the Martian surface, most of which are distributed in the southern highlands formed during the Noachian and Hesperian Epochs (Carter et al., 2013; Ehlmann and Edwards, 2014). Hydrated minerals have also been occasionally found in the younger northern lowlands, but they are mainly confined to excavated craters and were probably formed in more ancient periods (Carter et al., 2010; Pan L et al., 2017; Pan L and Ehlmann, 2018). The hydrated minerals detected by the Zhurong rover, probably sulfates or opaline silica, are mainly associated with light-toned rocks on the surface of Utopia Planitia in the northern lowlands (Liu Y et al., 2022). The morphology of these rocks is similar to the duricrust at the landing site of Viking 1 and was interpreted to be indigenously formed (Liu Y et al., 2022). The terrain at the landing site of the Zhurong rover has an absolute model age of 757 ± 66 Ma (Zhao JN et al., 2021). Therefore, the indigenous formation of hydrated minerals in southern Utopia Planitia suggests that aqueous activities were present during the mid-Amazonian on Mars.

5.2 Formation Mechanism of the Rocks and Environmental Implications

The Zhurong landing site is located in southern Utopia Planitia, which has a generally flat terrain. No evidence of fluvial networks or lacustrine environments exists in this area (Wu X et al., 2021; Ye

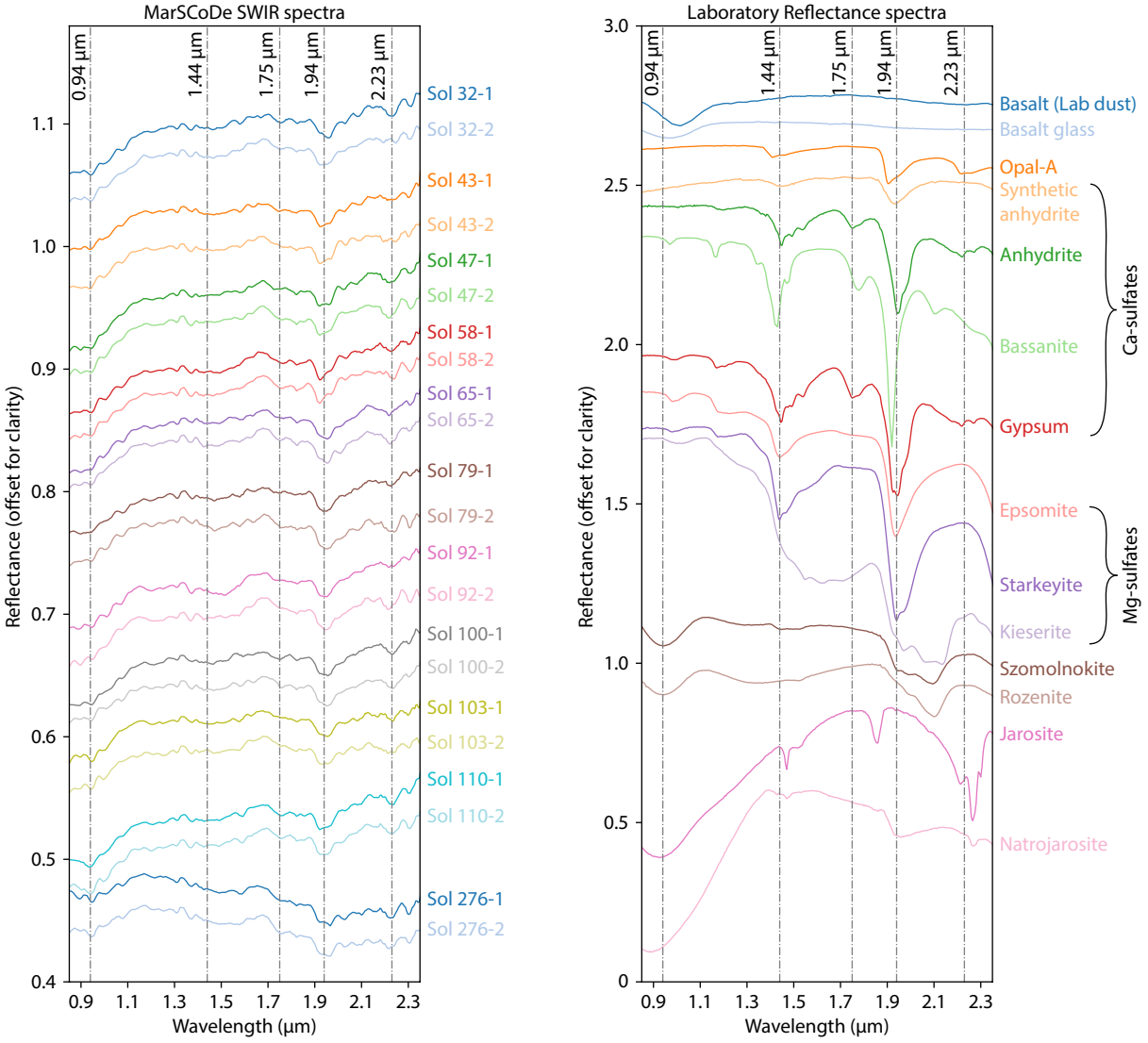

Figure 3. Short-wave infrared (SWIR) reflectance spectra from the Zhurong rover (left) with laboratory-measured spectra as references (right). Two different spectra from each sol represent the analyses of two targets in the same sol (Table S3). The sources of the reference spectra are listed in Table S5. The unsmoothed spectra are shown in Figure S1.

BL et al., 2021; Zhao JN et al., 2021). Instead, groundwater beneath the surface could be possible. Many pitted cones have been found around the landing site. Although the formation mechanism of pitted cones is still unclear (Wu X et al., 2021), groundwater activity could be a viable process (Ye BL et al., 2021). Thus, it is more likely that the hydrated minerals in the targeted samples were formed by groundwater. Episodic interaction of the igneous materials with groundwater may have resulted in the formation of sulfates or opaline silica. Aeolian processes may have eroded the original surface and exposed the rocks analyzed by the Zhurong rover.

The elemental compositions analyzed by LIBS may further constrain the water activity. Although the intensities for the H emission line in spectra from different targeted samples showed large variations (Figure 5), there were few differences in major elements (such as Ca and Si) between these samples. This result is in contrast to the observations by Curiosity's LIBS spectra at Gale crater, where the H signal was related to different types of targets, and samples with hydrated minerals (such as gypsum and bassanite with high Ca concentrations) typically showed more elevated H intensities than did igneous targets (Schröder et al., 2015). Additionally, semiquantitative elemental ratios had no significant variations (Figure 6), including the targets that were interpreted to be basaltic rocks (Sol 45-1 and Sol 50-1; Liu Y et al., 2022). And the overall spectra of the targeted samples by Zhurong were similar to that of the basalt reference (Figure 4). Thus, it is likely that no significant addition or depletion of major cation elements occurred during the formation of these rocks. Such a scenario is uncommon because the formation of hydrated minerals during weathering would lead to the depletion of mobile elements (such as Ca and Mg), and the addition of evaporites would cause enrichments of either Ca, Mg, or Si.

Observations by the Opportunity rover at Meridiani Planum bear some similarities to data from the Zhurong rover. The elemental compositions of the Meridiani bedrock closely resemble Martian basalts, with the addition of an extra S component (Rieder et al., 2004; McCollom and Hynek, 2005). These rocks were interpreted to be mixtures of siliciclastic materials and evaporites formed by groundwater (McLennan et al., 2005; Squyres et al., 2006),

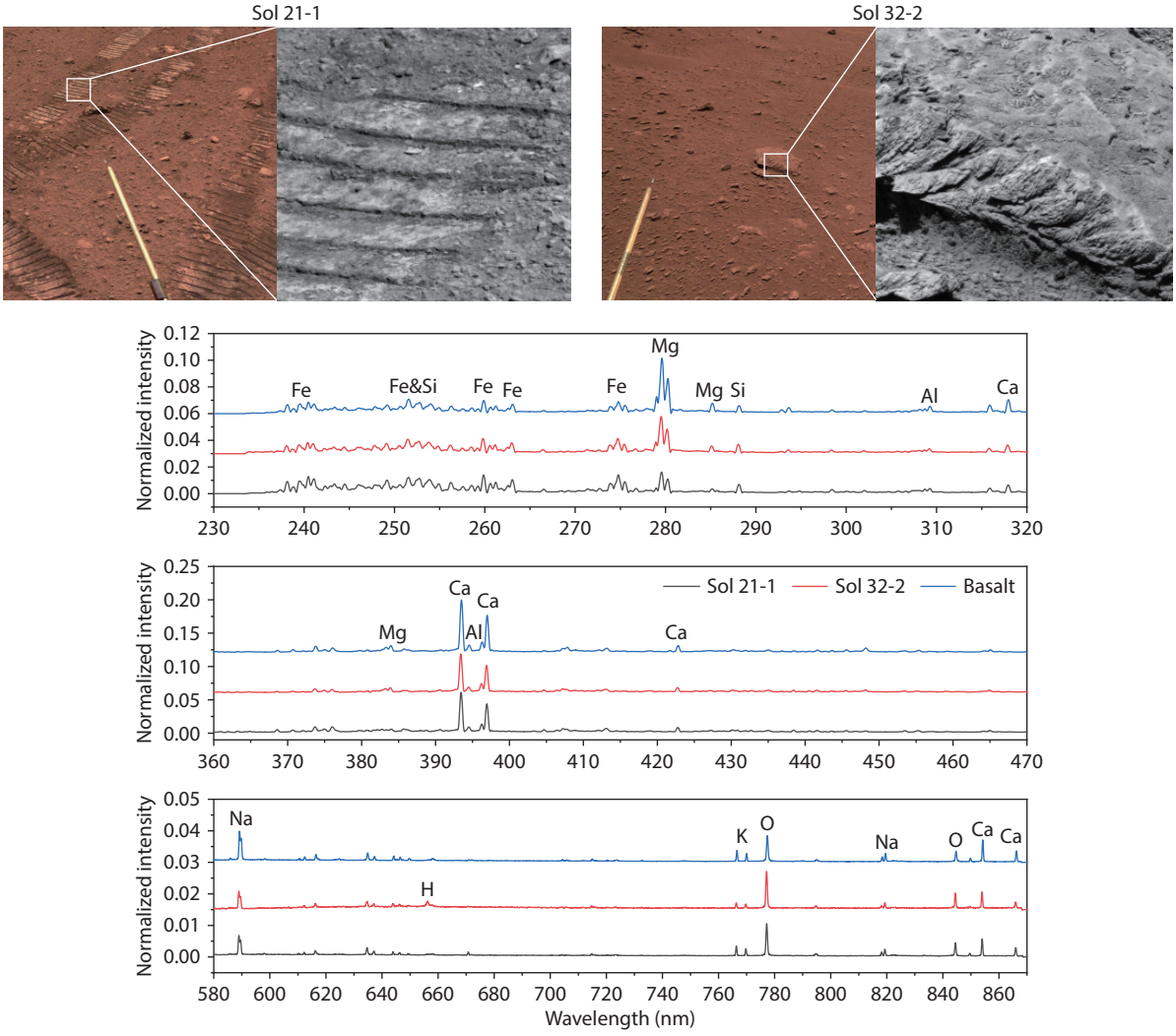

Figure 4. Typical laser-induced breakdown spectrometer (LIBS) spectra of two targets (Sol 21-1 and Sol 32-2) and a basalt reference. The images showing the targets are from the Navigation and Terrain Camera (NaTeCam, left) and the Multispectral Camera (MSCam, right, Table S4). Note that the scales of normalized intensities in the three wavelength ranges are different.

although controversy remains (McCollom and Hynek, 2005; Niles and Michalski, 2009). The similarity of major cations with Martian basalts was explained as that the pristine basaltic materials were first depleted of mobile cations (possibly during weathering) and then they regained these cations (and extra S) during the following evaporation of brine (Squyres et al., 2006). Due to the relatively low intensities of the S emission lines in the spectral range of LIBS (Nachon et al., 2014), the poor signal-to-noise ratios of the spectra hindered the detection of S in the targeted samples at the Zhurong landing site. Although we lack information on S concentrations in the samples, the scenario proposed for the Meridiani rocks may be difficult to achieve at the Zhurong landing site. Meridiani Planum is located in the southern highlands, which have a widespread distribution of phyllosilicates (Ehlmann and Edwards, 2014). It is plausible that the Meridiani rocks may have originated from previously weathered basaltic materials. In contrast, little evidence of chemical weathering exists in the northern lowlands (Ehlmann and Edwards, 2014). Therefore, it is too arbitrary to ascribe the basalt-like elemental compositions of the targeted samples by Zhurong to the depletion and readdition of cations during weathering and evaporation.

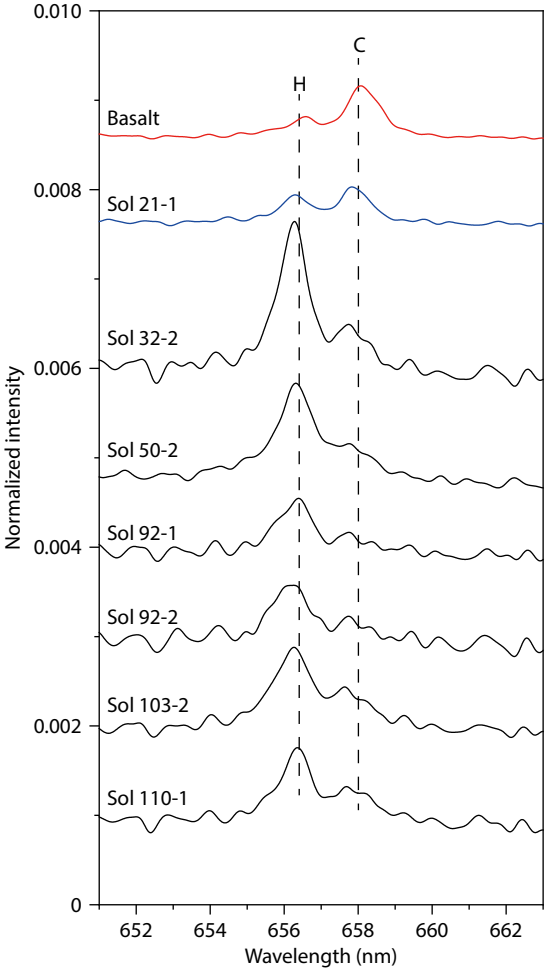

Figure 5. Six laser-induced breakdown spectrometer (LIBS) spectra with notably higher peaks for H at ~656.5 nm than the C peak at ~658 nm (black). Spectra from a typical target with a less obvious H signal (Sol 21-1) and a basalt reference are also shown.

A possible interpretation of the existence of hydrated minerals and overall basalt-like elemental compositions in the targeted samples is that no significant migration of elements occurred during the formation of the hydrated minerals. The elements in the hydrated minerals may be mostly from indigenous pristine igneous rocks, with little loss of elements or addition of elements from another reservoir during their formation. Thus, the observed samples would be mixtures of secondary minerals and weathering residues of indigenous igneous rocks, and the overall elemental compositions would be similar to those of the pristine igneous rocks. This could be achieved if there had been only a limited amount of standing groundwater to interact with the igneous materials in this area. In this scenario, fresh groundwater may have been injected into the studied site and interacted with basaltic debris. The evaporation of the water may then have led to the precipitation of sulfates or opaline silica, cementing the original materials. If the groundwater was limited in scale and duration, the migration of the water (and the dissolved elements) could be negligible. Thus, hydrated minerals may have been indigenously formed through water–rock interaction and later evaporation, and in this case, there would have been little addition or depletion of mobile elements. This may suggest that the water activity at the landing site during the Amazonian was on a restricted scale and of a short duration. This kind of water activity may be related to the melting of underground ice during occasional thermal events, such as impact or volcanism.

Nonetheless, the light-toned clast rocks and platy rocks observed along the traverse of the rover have various morphologies and are widely distributed in this area. The irregular shapes of the platy rocks are significantly different from those of igneous rocks (Figures 2d, 2e). These rocks have slab structures and are much larger than the clast rocks, which would be difficult to form through transient and restricted aqueous alteration of igneous rocks. It is also unclear whether the interaction between igneous clasts and a limited amount of water could result in the formation of layered structures in some rocks (Figure 2b). Instead, layered structures may require long-time alteration by fluctuating groundwater tables or sedimentary processes in a water body. The limited scale of water activities would make both scenarios difficult to achieve. Therefore, the scale and duration of water activities at the landing site remain an open question.

Because of the limited number of analyzed targets and the nonquantitative interpretation of the LIBS data in this work, we cannot reach an unambiguous conclusion on the formation mechanism of these rocks. Further more in-depth quantitative interpretation of the LIBS spectra and future investigation of more rock targets and other related geologic features by the Zhurong rover in southern Utopia Planitia may give more detailed constraints on the origin of the light-toned rocks and its implications for climate and environmental conditions during the Amazonian.

6. Conclusions

This study presents the mineralogical and elemental results from the MarSCoDe onboard the Zhurong rover, which landed in southern Utopia Planitia. The absorption bands of H_2O and OH from the SWIR spectra and the detection of high concentrations of

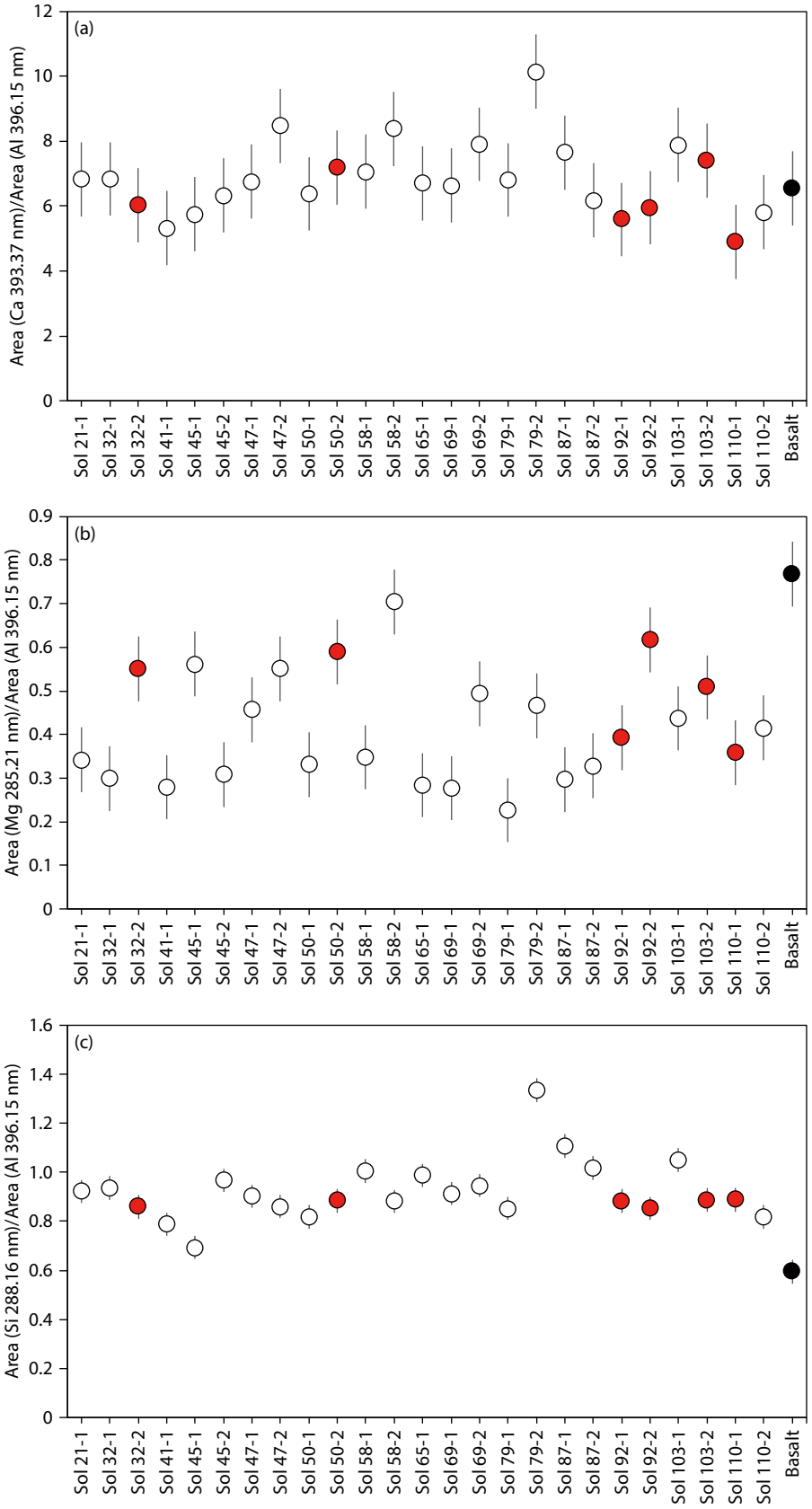

Figure 6. The integrated areas of emission lines from Ca/Al (a), Mg/Al (b), and Si/Al (c) for 25 laser-induced breakdown spectrometer (LIBS) spectra with reliable signal-to-noise ratios. The red circles are the six targets with notably high H peaks, and the black circle denotes the basalt reference. Error bars of the data are two standard deviations (2SD) of three replicate analyses for the basalt reference, which should be much smaller than the real uncertainties for the targeted samples because of their lower signal-to-noise ratios.

H in LIBS spectra suggest the presence of hydrated minerals (opaline silica or Ca- and Mg-sulfates) at the landing site. The discovery of hydrated minerals in southern Utopia Planitia suggests that liquid water activities were present during the overall cold and dry Amazonian era on Mars. However, the basalt-like elemental compositions of the analyzed targets indicate that the duration and scale of the water activities need further evaluation. This study suggests a more diverse hydrological condition during the Amazonian on Mars.

Acknowledgments

All the data presented in this work are archived on the Lunar and Planetary Data Release System (https://moon.bao.ac.cn/web/enmanager/home). We thank the Tianwen-1 team for operating a successful mission and providing the data set. We also thank Yang Liu for sharing the laboratory-measured reflectance value of the calibration panel, Lu Pan for help in wavelength correction, and Changqing Liu for the method of target calibration. This work was funded by the Strategic Priority Research Program (B) of Chinese Academy of Sciences (Grant No. XDB41000000), the National Natural Science Foundation of China (Grant No. 41930216), the Pre-research Project on Civil Aerospace Technologies (Grant No. D020202) of the Chinese National Space Administration, and the Fundamental Research Funds for the Central Universities of China (Grant No. WK3410000019).

References

Baird, A. K., Toulmin, P., Clark, B. C., Rose, H. J., Keil, K., Christian, R. P., and Gooding, J. L. (1976). Mineralogic and petrologic implications of Viking geochemical results from Mars: Interim report. *Science*, *194*(4271), 1288–1293. https://doi.org/10.1126/science.194.4271.1288

Bandfield, J. L., Amador, E. S., and Thomas, N. H. (2013). Extensive hydrated silica materials in western Hellas Basin, Mars. *Icarus*, *226*(2), 1489–1498. https://doi.org/10.1016/j.icarus.2013.08.005

Bibring, J. P., Langevin, Y., Mustard, J. F., Poulet, F., Arvidson, R., Gendrin, A., Gondet, B., Mangold, N., Pinet, P., ... Neukum, G. (2006). Global mineralogical and aqueous Mars history derived from OMEGA/Mars Express data. *Science*, *312*(5772), 400–404. https://doi.org/10.1126/science.1122659

Biemann, K., Oro, J., Toulmin, P., Orgel, L. E., Nier, A. O., Anderson, D. M., Simmonds, P. G., Flory, D., Diaz, A. V., ... Biller, J. A. (1976). Search for organic and volatile inorganic compounds in two surface samples from the Chryse Planitia region of Mars. *Science*, *194*(4260), 72–76. https://doi.org/10.1126/science.194.4260.72

Bishop, J. L., Schiffman, P., Lane, M. D., and Dyar, M. D. (2005). Solfataric alteration in Hawaii as a mechanism for formation of the sulfates observed on Mars by OMEGA and the MER instruments. In *36th Annual Lunar and Planetary Science Conference* (abstract 1456). League City, Texas.

Bishop, J. L., Dobrea, E. Z. N., McKeown, N. K., Parente, M., Ehlmann, B. L., Michalski, J. R., Milliken, R. E., Poulet, F., Swayze, G. A., ... Bibring, J. P. (2008). Phyllosilicate diversity and past aqueous activity revealed at Mawrth Vallis, Mars. *Science*, *321*(5890), 830–833. https://doi.org/10.1126/science.1159699

Bridges, J. C., and Grady, M. M. (2000). Evaporite mineral assemblages in the Nakhlite (Martian) meteorites. *Earth Planet. Sci. Lett.*, *176*(3–4), 267–279. https://doi.org/10.1016/S0012-821X(00)00019-4

Buczkowski, D. L., and Cooke, M. L. (2004). Formation of double-ring circular grabens due to volumetric compaction over buried impact craters: Implications for thickness and nature of cover material in Utopia Planitia, Mars. *J. Geophys. Res. Planets*, *109*(E2), E02006. https://doi.org/10.1029/2003JE002144

Bullock, M. A., Moore, J. M., and Mellon, M. T. (2004). Laboratory simulations of Mars aqueous geochemistry. *Icarus*, *170*(2), 404–423. https://doi.org/10.1016/j.icarus.2004.03.016

Burns, R. G., and Fisher, D. S. (1990). Iron–sulfur mineralogy of Mars: Magmatic evolution and chemical weathering products. *J. Geophys. Res.: Solid Earth*, *95*(B9), 14415–14421. https://doi.org/10.1029/JB095iB09p14415

Carter, J., Poulet, F., Bibring, J. P., Mangold, N., and Murchie, S. (2013). Hydrous minerals on Mars as seen by the CRISM and OMEGA imaging spectrometers: Updated global view. *J. Geophys. Res.: Planets*, *118*(4), 831–858. https://doi.org/10.1029/2012je004145

Carter, J., Poulet, F., Bibring, J. P., and Murchie, S. (2010). Detection of hydrated silicates in crustal outcrops in the northern plains of Mars. *Science*, *328*(5986), 1682–1686. https://doi.org/10.1126/science.1189013

Clark, B. C., and Van Hart, D. C. (1981). The salts of Mars. *Icarus*, *45*(2), 370–378. https://doi.org/10.1016/0019-1035(81)90041-5

Clark, R. N. (1999). Spectroscopy of rocks and minerals, and principles of spectroscopy. In A. N. Rencz (Ed.), *Manual of Remote Sensing, Volume 3, Remote Sensing for the Earth Sciences* (pp. 3–58). New York: Wiley.

Cloutis, E., Hawthorne, F., Mertzman, S., Krenn, K., Craig, M., Marcino, D., Methot, M., Strong, J., Mustard, J., ... Vilas, F. (2006). Detection and discrimination of sulfate minerals using reflectance spectroscopy. *Icarus*, *184*(1), 121–157. https://doi.org/10.1016/j.icarus.2006.04.003

de Pablo, M. Á., and Komatsu, G. (2009). Possible pingo fields in the Utopia basin, Mars: Geological and climatical implications. *Icarus*, *199*(1), 49–74. https://doi.org/10.1016/j.icarus.2008.09.007

Dickson, J. L., Lamb, M. P., Williams, R. M. E., Hayden, A. T., and Fischer, W. W. (2021). The global distribution of depositional rivers on early Mars. *Geology*, *49*(5), 504–509. https://doi.org/10.1130/G48457.1

Ehlmann, B. L., and Edwards, C. S. (2014). Mineralogy of the Martian surface. *Annu. Rev. Earth Planet. Sci.*, *42*, 291–315. https://doi.org/10.1146/annurev-earth-060313-055024

Fassett, C. I., and Head, J. W. (2011). Sequence and timing of conditions on early Mars. *Icarus*, *211*(2), 1204–1214. https://doi.org/10.1016/j.icarus.2010.11.014

Gendrin, A., Mangold, N., Bibring, J. P., Langevin, Y., Gondet, B., Poulet, F., Bonello, G., Quantin, C., Mustard, J., ... LeMouélic, S. (2005). Sulfates in Martian layered terrains: The OMEGA/Mars Express view. *Science*, *307*(5715), 1587–1591. https://doi.org/10.1126/science.1109087

Hamilton, V. E., McSween, H. Y., and Hapke, B. (2005). Mineralogy of Martian atmospheric dust inferred from thermal infrared spectra of aerosols. *J. Geophys. Res.: Planets*, *110*(E12), E12006. https://doi.org/10.1029/2005je002501

Head, J. W., III, Kreslavsky, M. A., and Pratt, S. (2002). Northern lowlands of Mars: Evidence for widespread volcanic flooding and tectonic deformation in the Hesperian Period. *J. Geophys. Res.: Planets*, *107*(E1), 5003. https://doi.org/10.1029/2000JE001445

Hu, X. Y., Ma, P., Yang, Y. Z., Zhu, M. H., Jiang, T., Lucey, P. G., Sun, L. Z., Zhang, H., Li, C. L., ... Sun, Y. X. (2019). Mineral abundances inferred from *in situ* reflectance measurements of Chang'E-4 landing site in South Pole-Aitken Basin. *Geophys. Res. Lett.*, *46*(16), 9439–9447. https://doi.org/10.1029/2019GL084531

Huang, H., Wang, X., Chen, Y., Zhang, Q., Zhao, F. Y., Ren, X., Zeng, X. G., Yan, W., Chen, W. L., ... Liu, J. J. (2023). Observations and interpretations of geomorphologic features in the Tianwen-1 landing area on Mars by using orbital imagery data. *Earth Planet. Phys.*, *7*(1), 1–16. https://doi.org/10.26464/epp2023005

Ivanov, M. A., Hiesinger, H., Erkeling, G., and Reiss, D. (2014). Mud volcanism and morphology of impact craters in Utopia Planitia on Mars: Evidence for the ancient ocean. *Icarus*, *228*, 121–140. https://doi.org/10.1016/j.icarus.2013.09.018

Johnson, S. S., Mischna, M. A., Grove, T. L., and Zuber, M. T. (2008). Sulfur-induced greenhouse warming on early Mars. *J. Geophys. Res.: Planets*, *113*(E8), E08005. https://doi.org/10.1029/2007JE002962

Knauth, L. P., and Burt, D. M. (2004). The "Brine Splat" hypothesis for features observed at the opportunity landing site. In *Second Conference on Early Mars: Geologic, Hydrologic, and Climatic Evolution and the Implications for Life*. Jackson Hole, Wyoming.

Lanz, J. K., Wagner, R., Wolf, U., Kröchert, J., and Neukum, G. (2010). Rift zone volcanism and associated cinder cone field in Utopia Planitia, Mars. *J. Geophys. Res.*: *Planets*, *115*(E12), E12019. https://doi.org/10.1029/2010JE003578

Lee, M. R., MacLaren, I., Andersson, S. M. L., Kovács, A., Tomkinson, T., Mark, D. F., and Smith, C. L. (2015). Opal-A in the Nakhla meteorite: A tracer of ephemeral liquid water in the Amazonian crust of Mars. *Meteorit. Planet. Sci*, *50*(8), 1362–1377. https://doi.org/10.1111/maps.12471

Li, C., Zheng, Y. K., Wang, X., Zhang, J. H., Wang, Y. B., Chen, L., Zhang, L., Zhao, P., Liu, Y. K., ... Wu, F. Y. (2022). Layered subsurface in Utopia Basin of Mars revealed by Zhurong rover radar. *Nature*, *610*(7931), 308–312. https://doi.org/10.1038/s41586-022-05147-5

Liu, J. J., Li, C. L., Zhang, R. Q., Rao, W., Cui, X. F., Geng, Y., Jia, Y., Huang, H., Ren, X., ... Zhang, H. B. (2022). Geomorphic contexts and science focus of the Zhurong landing site on Mars. *Nat. Astron.*, *6*(1), 65–71. https://doi.org/10.1038/s41550-021-01519-5

Liu, Y., Goudge, T. A., Catalano, J. G., and Wang, A. (2018). Spectral and stratigraphic mapping of hydrated minerals associated with interior layered deposits near the southern wall of Melas Chasma, Mars. *Icarus*, *302*, 62–79. https://doi.org/10.1016/j.icarus.2017.11.006

Liu, Y., Wu, X., Zhao, Y. Y. S., Pan, L., Wang, C., Liu, J., Zhao, Z. X., Zhou, X., Zhang, C. L., ... Zou, Y. L. (2022). Zhurong reveals recent aqueous activities in Utopia Planitia, Mars. *Sci. Adv.*, *8*(19), eabn8555. https://doi.org/10.1126/sciadv.abn8555

Lu, Y., Edgett, K. S., Wu, B., Wang, Y. R., Li, Z. J., Michael, G. G., Yizhaq, H., Jin, Q., and Wu, Y. Z. (2022). Aeolian disruption and reworking of TARs at the Zhurong rover field site, southern Utopia Planitia, Mars. *Earth Planet. Sci. Lett.*, *595*, 117785. https://doi.org/10.1016/j.epsl.2022.117785

Maurice, S., Clegg, S. M., Wiens, R. C., Gasnault, O., Rapin, W., Forni, O., Cousin, A., Sautter, V., Mangold, N., ... Vasavada, A. R. (2016). ChemCam activities and discoveries during the nominal mission of the Mars Science Laboratory in Gale crater, Mars. *J. Anal. Atom. Spectrom.*, *31*(4), 863–889. https://doi.org/10.1039/C5JA00417A

McCollom, T. M., and Hynek, B. M. (2005). A volcanic environment for bedrock diagenesis at Meridiani Planum on Mars. *Nature*, *438*(7071), 1129–1131. https://doi.org/10.1038/nature04390

McGill, G. E. (1989). Buried topography of Utopia, Mars: Persistence of a giant impact depression. *J. Geophys. Res.*: *Solid Earth*, *94*(B3), 2753–2759. https://doi.org/10.1029/JB094iB03p02753

McLennan, S. M., Bell, J. F., Calvin, W. M., Christensen, P. R., Clark, B. C., de Souza, P. A., Farmer, J., Farrand, W. H., Fike, D. A., ... Yen, A. (2005). Provenance and diagenesis of the evaporite-bearing Burns formation, Meridiani Planum, Mars. *Earth Planet. Sci. Lett.*, *240*(1), 95–121. https://doi.org/10.1016/j.epsl.2005.09.041

McLennan, S. M., Grotzinger, J. P., Hurowitz, J. A., and Tosca, N. J. (2019). The sedimentary cycle on Early Mars. *Annu. Rev. Earth Planet. Sci.*, *47*, 91–118. https://doi.org/10.1146/annurev-earth-053018-060332

Meslin, P. Y., Gasnault, O., Forni, O., Schröder, S., Cousin, A., Berger, G., Clegg, S. M., Lasue, J., Maurice, S., and Sautter, V. (2013). Soil diversity and hydration as observed by ChemCam at Gale Crater, Mars. *Science*, *341*(6153), 1238670. https://doi.org/10.1126/science.1238670

Milliken, R. E., Swayze, G. A., Arvidson, R. E., Bishop, J. L., Clark, R. N., Ehlmann, B. L., Green, R. O., Grotzinger, J. P., Morris, R. V., ... Weitz, C. (2008). Opaline silica in young deposits on Mars. *Geology*, *36*(11), 847–850. https://doi.org/10.1130/G24967A.1

Mills, M. M., McEwen, A. S., and Okubo, C. H. (2021). A preliminary regional geomorphologic map in Utopia Planitia of the Tianwen-1 Zhurong landing region. *Geophys. Res. Lett.*, *48*(18), e2021GL094629. https://doi.org/10.1029/2021GL094629

Minitti, M. E., Weitz, C. M., Lane, M. D., and Bishop, J. L. (2007). Morphology, chemistry, and spectral properties of Hawaiian rock coatings and implications for Mars. *J. Geophys. Res.*: *Planets*, *112*(E5), E05015. https://doi.org/10.1029/2006JE002839

Nachon, M., Clegg, S. M., Mangold, N., Schröder, S., Kah, L. C., Dromart, G., Ollila, A., Johnson, J. R., Oehler, D. Z., ... Wellington, D. (2014). Calcium sulfate veins characterized by ChemCam/Curiosity at Gale crater, Mars. *J. Geophys. Res.*: *Planets*, *119*(9), 1991–2016. https://doi.org/10.1002/2013JE004588

Nesbitt, H. W., and Wilson, R. E. (1992). Recent chemical weathering of basalts. *Am. J. Sci.*, *292*(10), 740–777. https://doi.org/10.2475/ajs.292.10.740

Newsom, H. E., Hagerty, J. J., and Goff, F. (1999). Mixed hydrothermal fluids and the origin of the Martian soil. *J. Geophys. Res.*: *Planets*, *104*(E4), 8717–8728. https://doi.org/10.1029/1998JE900043

Niles, P. B., and Michalski, J. (2009). Meridiani Planum sediments on Mars formed through weathering in massive ice deposits. *Nat. Geosci.*, *2*(3), 215–220. https://doi.org/10.1038/ngeo438

Pan, L., Ehlmann, B. L., Carter, J., and Ernst, C. M. (2017). The stratigraphy and history of Mars' northern lowlands through mineralogy of impact craters: A comprehensive survey: Stratigraphy of Mars' Northern Lowlands. *J. Geophys. Res.*: *Planets*, *122*(9), 1824–1854. https://doi.org/10.1002/2017JE005276

Pan, L., and Ehlmann, B. L. (2018). Aqueous processes from diverse hydrous minerals in the vicinity of Amazonian-aged Lyot crater. *J. Geophys. Res.*: *Planets*, *123*(7), 1618–1648. https://doi.org/10.1029/2017JE005461

Rapin, W., Meslin, P. Y., Maurice, S., Vaniman, D., Nachon, M., Mangold, N., Schröder, S., Gasnault, O., Forni, O., ... Rampe, E. B. (2016). Hydration state of calcium sulfates in Gale crater, Mars: Identification of bassanite veins. *Earth Planet. Sci. Lett.*, *452*, 197–205. https://doi.org/10.1016/j.epsl.2016.07.045

Rieder, R., Gellert, R., Anderson, R. C., Brückner, J., Clark, B. C., Dreibus, G., Economou, T., Klingelhöfer, G., Lugmair, G. W., ... Zipfel, J. (2004). Chemistry of rocks and soils at Meridiani Planum from the Alpha Particle X-ray Spectrometer. *Science*, *306*(5702), 1746–1749. https://doi.org/10.1126/science.110435

Ruff, S. W., Farmer, J. D., Calvin, W. M., Herkenhoff, K. E., Johnson, J. R., Morris, R. V., Rice, M. S., Arvidson, R. E., Bell, J. F., III, ... Squyres, S. W. (2011). Characteristics, distribution, origin, and significance of opaline silica observed by the Spirit rover in Gusev crater, Mars. *J. Geophys. Res.*: *Planets*, *116*(E7), E00F23. https://doi.org/10.1029/2010JE003767

Savitzky, A., and Golay, M. J. E. (1964). Smoothing and differentiation of data by simplified least squares procedures. *Anal. Chem.*, *36*(8), 1627–1639. https://doi.org/10.1021/ac60214a047

Schröder, S., Meslin, P. Y., Gasnault, O., Maurice, S., Cousin, A., Wiens, R. C., Rapin, W., Dyar, M. D., Mangold, N., ... Vaniman, D. (2015). Hydrogen detection with ChemCam at Gale crater. *Icarus*, *249*, 43–61. https://doi.org/10.1016/j.icarus.2014.08.029

Settle, M. (1979). Formation and deposition of volcanic sulfate aerosols on Mars. *J. Geophys. Res.*: *Planets*, *84*(B14), 8343. https://doi.org/10.1029/JB084iB14p08343

Skok, J. R., Mustard, J. F., Ehlmann, B. L., Milliken, R. E., and Murchie, S. L. (2010). Silica deposits in the Nili Patera caldera on the Syrtis Major volcanic complex on Mars. *Nat. Geosci.*, *3*(12), 838–841. https://doi.org/10.1038/ngeo990

Squyres, S. W., Knoll, A. H., Arvidson, R. E., Clark, B. C., Grotzinger, J. P., Jolliff, B. L., McLennan, S. M., Tosca, N., Bell, J. F., III, ... Yen, A. S. (2006). Two years at Meridiani Planum: Results from the Opportunity Rover. *Science*, *313*(5792), 1403–1407. https://doi.org/10.1126/science.1130890

Sun, V. (2017). Clays and opals on Mars: Implications for water–rock interactions through time [Ph. D. thesis]. Brown University. https://doi.org/10.7301/Z08G8J58

Tanaka, K. L., Robbins, S. J., Fortezzo, C. M., Skinner, Jr. J. A., and Hare, T. M. (2014). The digital global geologic map of Mars: Chronostratigraphic ages, topographic and crater morphologic characteristics, and updated resurfacing history. *Planet. Space Sci.*, *95*, 11–24. https://doi.org/10.1016/j.pss.2013.03.006

Tosca, N. J., and Knoll, A. H. (2009). Juvenile chemical sediments and the long term persistence of water at the surface of Mars. *Earth Planet. Sci. Lett.*, *286*(3–4), 379–386. https://doi.org/10.1016/j.epsl.2009.07.004

Wu, B., Liu, C. Y., Xu, R., Lin, H. L., Xu, X. S., Yan, W., Tan, Y. J., Liu, B., Ren, X., ... Shu, R. (2022). Initial in-flight spectral calibration of the near-infrared spectra acquired by the MarSCoDe onboard the Zhurong rover. *Remote Sens.*, *14*(9), 2137. https://doi.org/10.3390/rs14092137

Wu, X., Liu, Y., Zhang, C. L., Wu, Y. C., Zhang, F., Du, J., Liu, Z. H., Xing, Y., Xu, R., ... Zou, Y. L. (2021). Geological characteristics of China's Tianwen-1 landing site at Utopia Planitia, Mars. *Icarus*, *370*, 114657. https://doi.org/10.1016/j.

icarus.2021.114657

Xu, W. M., Liu, X. F., Yan, Z. X., Li, L. N., Zhang, Z. Q., Kuang, Y. W., Jiang, H., Yu, H. X., Yang, F., ... Shu, R. (2021). The MarSCoDe instrument suite on the Mars rover of China's Tianwen-1 mission. *Space Sci. Rev.*, *217*(5), 64. https://doi.org/10.1007/s11214-021-00836-5

Ye, B. L., Qian, Y. Q., Xiao, L., Michalski, J. R., Li, Y. L., Wu, B., and Qiao, L. (2021). Geomorphologic exploration targets at the Zhurong landing site in the southern Utopia Planitia of Mars. *Earth Planet. Sci. Lett.*, *576*, 117199. https://doi.org/10.1016/j.epsl.2021.117199

Ye, C., Sklute, E. C., and Glotch, T. D. (2021). Orientation averaged visible/near-infrared and mid-infrared optical constants of hydrous Ca-sulfates: Gypsum and bassanite. *Earth Space Sci.*, *8*. https://doi.org/10.1029/2021EA001834

Yen, A. S., Gellert, R., Schröder, C., Morris, R. V., Bell, J. F., III, Knudson, A. T., Clark, B. C., Ming, D. W., Crisp, J. A., ... Zipfel, J. (2005). An integrated view of the chemistry and mineralogy of Martian soils. *Nature*, *436*(7047), 49–54. https://doi.org/10.1038/nature03637

Zhao, J. N., Xiao, Z. J., Huang, J., Head, J. W., Wang, J., Shi, Y. T., Wu, B., and Wang, L. (2021). Geological characteristics and targets of high scientific interest in the Zhurong landing region on Mars. *Geophys. Res. Lett.*, *48*(20), e2021GL094903. https://doi.org/10.1029/2021GL094903

Zou, Y. L., Zhu, Y., Bai, Y. F., Wang, L. G., Jia, Y. Z., Shen, W. H., Fan, Y., Liu, Y., Wang, C., ... Peng, Y. Q. (2021). Scientific objectives and payloads of Tianwen-1, China's first Mars exploration mission. *Adv. Space Res.*, *67*(2), 812–823. https://doi.org/10.1016/j.asr.2020.11.005

Supplementary Materials for "Constraints on water activity at the Zhurong landing site in Utopia Planitia, Mars"

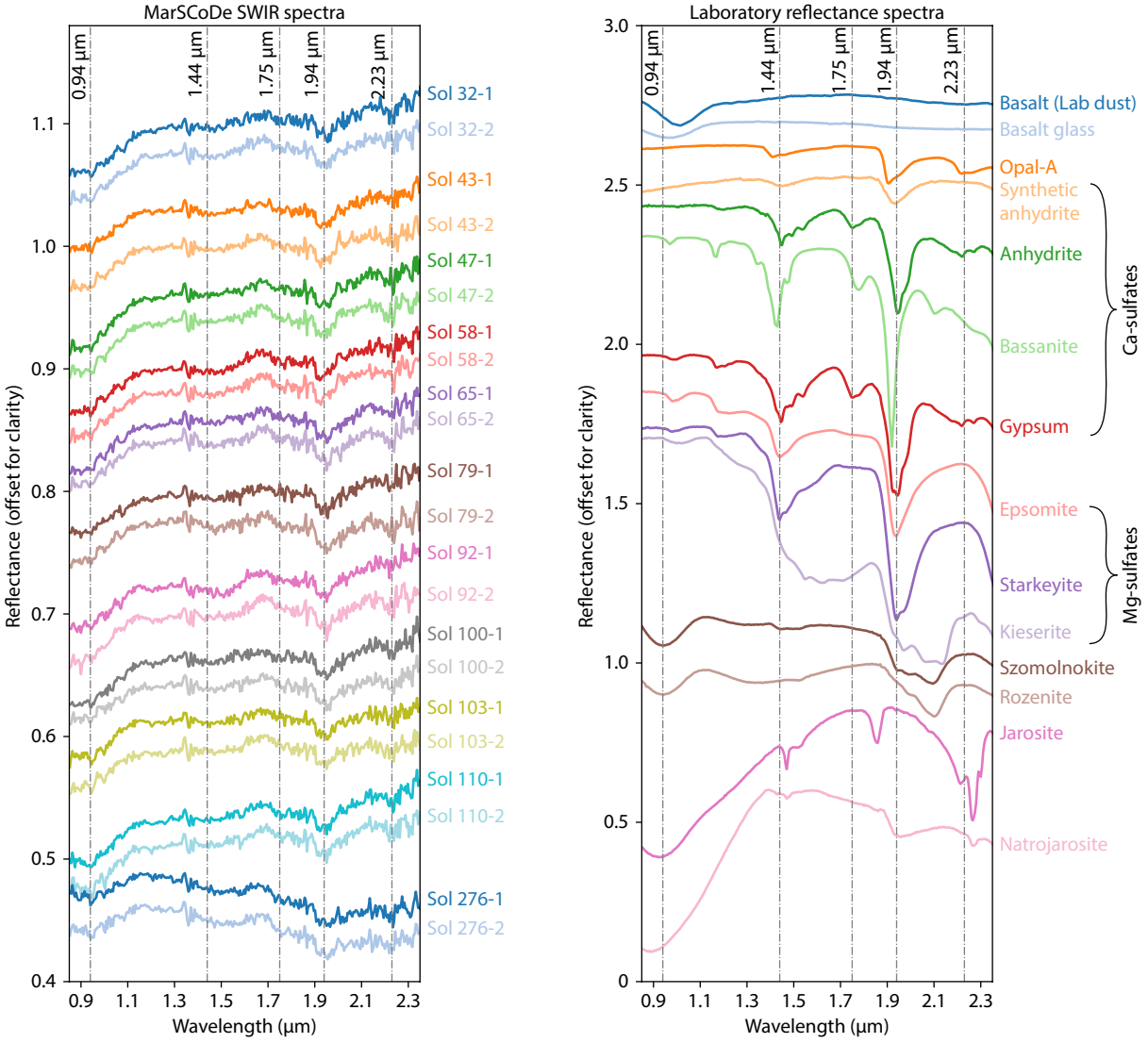

Figure S1. The Mars Surface Composition Detector (MarSCoDe) short-wave infrared (SWIR) spectra after the wavelength correction without denoising (left) and laboratory-measured spectra (right). Note that the angle configurations (incidence and emission angles) of MarSCoDe are different from those in the Reflectance Experiment Laboratory (RELAB) data set. Most of the incidence angles are less than 20°. The emission angles could be estimated as 48° to 76° because the distance from the pointing mirror to the ground is approximately 1 m, and the distances from the pointing mirror to targets are 1.5 to 4.2 m. Further laboratory studies are needed to shed light on the effect of angle configurations.

Table S1. The High-Resolution Imaging Camera (HiRIC) data used in this work.

Type	File name
Digital elevation model	HX1_GRAS_HIRIC_DEM_3.5_0000_244453N1101905E_A.tif
Digital image model	HX1_GRAS_HIRIC_DIM_0.7_0004_251515N1095850E_A.tif

Table S2. The Navigation and Terrain Camera (NaTeCam) data used in this work.

Sol	File name
20	HX1-Ro_GRAS_NaTeCamB-F-006_SCI_N_20210603091004_20210603091004_00020_A.2C
22	HX1-Ro_GRAS_NaTeCamA-F-001_SCI_N_20210605105115_20210605105115_00022_A.2C
31	HX1-Ro_GRAS_NaTeCamA-F-003_SCI_N_20210614164834_20210614164834_00031_A.2C
42	HX1-Ro_GRAS_NaTeCamA-F-001_SCI_N_20210625233144_20210625233144_00042_A.2C
91	HX1-Ro_GRAS_NaTeCamA-F-001_SCI_N_20210815054820_20210815054820_00091_A.2C
113	HX1-Ro_GRAS_NaTeCamA-F-001_SCI_N_20210906222131_20210906222131_00113_A.2C
172	HX1-Ro_GRAS_NaTeCamA-F-002_SCI_N_20211106122955_20211106122955_00172_A.2C
274	HX1-Ro_GRAS_NaTeCamB-F-003_SCI_N_20220219070045_20220219070045_00274_A.2C

Table S3. The Mars Surface Composition Detector (MarSCoDe) data used in this work.

Type[a]	Sol	File name
SWIR science data	32	HX1-Ro_GRAS_MarSCoDe-SWIR321-05_SCI_N_20210615174231_20210615174231_00032_A.2B
		HX1-Ro_GRAS_MarSCoDe-SWIR321-06_SCI_N_20210615175431_20210615175431_00032_A.2B
	43	HX1-Ro_GRAS_MarSCoDe-SWIR321-06_SCI_N_20210627000435_20210627000435_00043_A.2B
		HX1-Ro_GRAS_MarSCoDe-SWIR321-07_SCI_N_20210627001222_20210627001222_00043_A.2B
	47	HX1-Ro_GRAS_MarSCoDe-SWIR321-06_SCI_N_20210701024155_20210701024155_00047_A.2B
		HX1-Ro_GRAS_MarSCoDe-SWIR321-07_SCI_N_20210701024942_20210701024942_00047_A.2B
	58	HX1-Ro_GRAS_MarSCoDe-SWIR321-07_SCI_N_20210712091850_20210712091850_00058_A.2B
		HX1-Ro_GRAS_MarSCoDe-SWIR321-08_SCI_N_20210712093241_20210712093241_00058_A.2B
	65	HX1-Ro_GRAS_MarSCoDe-SWIR321-06_SCI_N_20210719164905_20210719164905_00065_A.2B
		HX1-Ro_GRAS_MarSCoDe-SWIR321-07_SCI_N_20210719170256_20210719170256_00065_A.2B
	79	HX1-Ro_GRAS_MarSCoDe-SWIR321-06_SCI_N_20210803020034_20210803020034_00079_A.2B
		HX1-Ro_GRAS_MarSCoDe-SWIR321-07_SCI_N_20210803021425_20210803021425_00079_A.2B
	92	HX1-Ro_GRAS_MarSCoDe-SWIR321-06_SCI_N_20210816094511_20210816094511_00092_A.2B
		HX1-Ro_GRAS_MarSCoDe-SWIR321-07_SCI_N_20210816095902_20210816095902_00092_A.2B
	100	HX1-Ro_GRAS_MarSCoDe-SWIR321-06_SCI_N_20210824142652_20210824142652_00100_A.2B
		HX1-Ro_GRAS_MarSCoDe-SWIR321-07_SCI_N_20210824144043_20210824144043_00100_A.2B
	103	HX1-Ro_GRAS_MarSCoDe-SWIR321-06_SCI_N_20210827161812_20210827161812_00103_A.2B
		HX1-Ro_GRAS_MarSCoDe-SWIR321-07_SCI_N_20210827163203_20210827163203_00103_A.2B
	110	HX1-Ro_GRAS_MarSCoDe-SWIR321-06_SCI_N_20210903205115_20210903205115_00110_A.2B
		HX1-Ro_GRAS_MarSCoDe-SWIR321-07_SCI_N_20210903210506_20210903210506_00110_A.2B
	276	HX1-Ro_GRAS_MarSCoDe-SWIR321-04_SCI_N_20220221084848_20220221084848_00276_A.2B
		HX1-Ro_GRAS_MarSCoDe-SWIR321-05_SCI_N_20220221090239_20220221090239_00276_A.2B

Continued from Table S3

Type[a]	Sol	File name
SWIR calibration data	32	HX1-Ro_GRAS_MarSCoDe-SWIR321-03_CAL_N_20210615172503_20210615172503_00032_A.2B
	43	HX1-Ro_GRAS_MarSCoDe-SWIR321-04_CAL_N_20210626233426_20210626233426_00043_A.2B
	47	HX1-Ro_GRAS_MarSCoDe-SWIR321-04_CAL_N_20210701021146_20210701021146_00047_A.2B
	58	HX1-Ro_GRAS_MarSCoDe-SWIR321-04_CAL_N_20210712085350_20210712085350_00058_A.2B
	65	HX1-Ro_GRAS_MarSCoDe-SWIR321-04_CAL_N_20210719162405_20210719162405_00065_A.2B
	79	HX1-Ro_GRAS_MarSCoDe-SWIR321-04_CAL_N_20210803013534_20210803013534_00079_A.2B
	92	HX1-Ro_GRAS_MarSCoDe-SWIR321-04_CAL_N_20210816092217_20210816092217_00092_A.2B
	100	HX1-Ro_GRAS_MarSCoDe-SWIR321-04_CAL_N_20210824140341_20210824140341_00100_A.2B
	103	HX1-Ro_GRAS_MarSCoDe-SWIR321-04_CAL_N_20210827155518_20210827155518_00103_A.2B
	110	HX1-Ro_GRAS_MarSCoDe-SWIR321-04_CAL_N_20210903202821_20210903202821_00110_A.2B
	276	HX1-Ro_GRAS_MarSCoDe-SWIR321-02_CAL_N_20220221083145_20220221083145_00276_A.2B
LIBS science data	21	HX1-Ro_GRAS_MarSCoDe-LIBS-I-06_SCI_N_20210604132442_20210604132502_00021_A.2B
	32	HX1-Ro_GRAS_MarSCoDe-LIBS-I-05_SCI_N_20210615173712_20210615173733_00032_A.2B
		HX1-Ro_GRAS_MarSCoDe-LIBS-I-06_SCI_N_20210615174910_20210615174931_00032_A.2B
	41	HX1-Ro_GRAS_MarSCoDe-LIBS-I-06_SCI_N_20210625034210_20210625034231_00041_A.2B
	45	HX1-Ro_GRAS_MarSCoDe-LIBS-I-06_SCI_N_20210629073102_20210629073123_00045_A.2B
		HX1-Ro_GRAS_MarSCoDe-LIBS-I-07_SCI_N_20210629074321_20210629074342_00045_A.2B
	47	HX1-Ro_GRAS_MarSCoDe-LIBS-I-06_SCI_N_20210701022936_20210701022957_00047_A.2B
		HX1-Ro_GRAS_MarSCoDe-LIBS-I-07_SCI_N_20210701024155_20210701024216_00047_A.2B
	50	HX1-Ro_GRAS_MarSCoDe-LIBS-I-06_SCI_N_20210704104745_20210704104806_00050_A.2B
		HX1-Ro_GRAS_MarSCoDe-LIBS-I-07_SCI_N_20210704110004_20210704110025_00050_A.2B
	58	HX1-Ro_GRAS_MarSCoDe-LIBS-I-07_SCI_N_20210712091310_20210712091331_00058_A.2B
		HX1-Ro_GRAS_MarSCoDe-LIBS-I-08_SCI_N_20210712092659_20210712092720_00058_A.2B
	65	HX1-Ro_GRAS_MarSCoDe-LIBS-I-06_SCI_N_20210719164325_20210719164346_00065_A.2B
	69	HX1-Ro_GRAS_MarSCoDe-LIBS-I-06_SCI_N_20210723192057_20210723192118_00069_A.2B
		HX1-Ro_GRAS_MarSCoDe-LIBS-I-07_SCI_N_20210723193446_20210723193507_00069_A.2B
	79	HX1-Ro_GRAS_MarSCoDe-LIBS-I-06_SCI_N_20210803015454_20210803015515_00079_A.2B
		HX1-Ro_GRAS_MarSCoDe-LIBS-I-07_SCI_N_20210803020843_20210803020904_00079_A.2B
	87	HX1-Ro_GRAS_MarSCoDe-LIBS-I-06_SCI_N_20210811071011_20210811071032_00087_A.2B
		HX1-Ro_GRAS_MarSCoDe-LIBS-I-07_SCI_N_20210811072400_20210811072421_00087_A.2B
	92	HX1-Ro_GRAS_MarSCoDe-LIBS-I-06_SCI_N_20210816093931_20210816093952_00092_A.2B
		HX1-Ro_GRAS_MarSCoDe-LIBS-I-07_SCI_N_20210816095320_20210816095341_00092_A.2B
	103	HX1-Ro_GRAS_MarSCoDe-LIBS-I-06_SCI_N_20210827161232_20210827161253_00103_A.2B
		HX1-Ro_GRAS_MarSCoDe-LIBS-I-07_SCI_N_20210827162621_20210827162642_00103_A.2B
	110	HX1-Ro_GRAS_MarSCoDe-LIBS-I-06_SCI_N_20210903204535_20210903204556_00110_A.2B
		HX1-Ro_GRAS_MarSCoDe-LIBS-I-07_SCI_N_20210903205924_20210903205945_00110_A.2B
LIBS calibration data	43	HX1-Ro_GRAS_MarSCoDe-LIBS-I-03_CAL_N_20210626232844_20210626232905_00043_A.2B
	100	HX1-Ro_GRAS_MarSCoDe-LIBS-I-03_CAL_N_20210824135800_20210824135821_00100_A.2B
	110	HX1-Ro_GRAS_MarSCoDe-LIBS-I-03_CAL_N_20210903202240_20210903202301_00110_A.2B

[a] SWIR, short-wave infrared (spectrometer); LIBS, laser-induced breakdown spectrometer.

Table S4. The Multispectral Camera (MSCam) data used in this work.

Sol	File name
21	HX1-Ro_GRAS_MSCam-W-1-28-0001-05_SCI_N_20210604124714_20210604124714_00021_A.2B
32	HX1-Ro_GRAS_MSCam-W-1-36-0001-05_SCI_N_20210615165943_20210615165943_00032_A.2B

Table S5. Laboratory-measured visible and near-infrared spectra.

Mineral	Formula	Source[a]	ID
Basalt (lab dust)		RELAB	CABA02
Basalt glass		RELAB	C1BE70
Opal-A	$SiO_2 \cdot nH_2O$	(Sun, V 2017)	(B-10)B_a1
Synthetic anhydrite	$CaSO_4$	RELAB	CAEC02
Anhydrite	$CaSO_4$	RELAB	CAEC02
Bassanite	$CaSO_4 \cdot 0.5H_2O$	(Ye C et al., 2021)	bassanite_vnir_reflectance_sml
Gypsum	$CaSO_4 \cdot 2H_2O$	RELAB	C1CC33
Epsomite	$MgSO_4 \cdot 7H_2O$	RELAB	799F366
Starkeyite	$MgSO_4 \cdot 4H_2O$	RELAB	C1JB711
Kieserite	$MgSO_4 \cdot H_2O$	RELAB	C1CC15
Szomolnokite	$FeSO_4 \cdot H_2O$	RELAB	C1JB622A
Rozenite	$FeSO_4 \cdot 4H_2O$	RELAB	C1JB623A
Jarosite	$KFe_3(SO_4)_2(OH)_6$	RELAB	CASF29
Natrojarosite	$NaFe_3(SO_4)_2(OH)_6$	RELAB	CASF28

[a] RELAB, Reflectance Experiment Laboratory.